Geophysical Journal International

Geophys. J. Int. (2013) **194,** 488–498 doi: 10.1093/gji/ggt104
Advance Access publication 2013 April 16

Direct estimation of near-surface damping based on normalized energy density

Hiroyuki Goto,[1] Yuichi Kawamura,[2] Sumio Sawada[3] and Takashi Akazawa[4]

[1] *Disaster Prevention Research Institute, Kyoto University, Gokasho, Uji, Kyoto, Japan. E-mail: goto@catfish.dpri.kyoto-u.ac.jp*
[2] *Graduate school of Engineering, Kyoto University, Gokasho, Uji, Kyoto, Japan*
[3] *Disaster Prevention Research Institute, Kyoto University, Gokasho, Uji, Kyoto, Japan*
[4] *Geo-Research Institute,* 4-3-2 *Itachibori, Nishiku, Osaka, Japan*

Accepted 2013 March 18. Received 2013 March 10; in original form 2012 November 5

SUMMARY

We propose a direct estimation of dampings in surface layers based on the normalized energy density (NED). The ratio of the NED, defined as the NED for the uppermost layer divided by the NED for the basement, correlates well with the total damping, t_S^*. We apply the relation between the NED ratio and the total damping to estimate the total damping at an actual site, Katagihara (KTG) site in Japan. The total damping at the KTG site is directly estimated as $t_S^* = 0.038$. This value agrees well with the estimated values determined from a conventional method, incorporating the non-linear inversion scheme.

Key words: Earthquake ground motion; Seismic attenuation; Site effects; Wave propagation.

Downloaded from http://gji.oxfordjournals.org/ at Kyoto University Library on July 17, 2013

1 INTRODUCTION

The evaluation of site amplification is an important issue to be addressed in earthquake disaster mitigation in the field of Earthquake Engineering, for example, seismic microzonation (Borcherdt 1970), because it is one of the major factors causing damages to specific sites. For example, the basin-edge effect (Kawase 1996) causes the spatial anomaly of damage distributions, such as that which occurred in Mexico City during the 1985 Michoacan, Mexico, earthquake (Kawase & Aki 1989), in the 'damage belt' during the 1995 Kobe, Japan, earthquake (Kawase 1996), in Adapazari during the 1999 Kocaeli, Turkey, earthquake (Goto *et al.* 2005), in Tomakomai in the Yufutsu basin during the 2003 Tokachi-oki, Japan, earthquake (Hatayama *et al.* 2007), etc. In some cases, the damaged areas were located far from the seismic faults. The non-linear site response is another factor to cause a damage; it is sometimes associated with the liquefaction of saturated sands, as observed during the 1993 Kushiro-oki, Japan, earthquake (Iai *et al.* 1995), during the 1995 Kobe earthquake (Suetomi & Yoshida 1998), and also during the 2011 off the Pacific coast of Tohoku, Japan, earthquake (Goto *et al.* 2012; Goto & Morikawa 2012).

The site amplification has been evaluated from several types of approaches. When geophysical exploration traces and also the other survey data (e.g. microtremor arrays, gravity anomaly, etc.) are available, a 3-D basin model can be numerically constructed, for example, Kagawa *et al.* (2004a), and the model can be verified and updated by a comparison with the ground motion records, for example, Iwaki & Iwata (2010). This approach is the most appropriate for evaluating the site amplification; however it is too costly to apply in dealing with the whole region of the Earth. Another approach is to interpolate the characteristics of the site amplification based on geological and geophysical information, for example, a Vs^{30} map evaluated from the geomorphologic classification (Wakamatsu & Matsuoka 2006; Wald & Allen 2007). It is possible to obtain a map of the amplification in the scale of the Earth; however, users should understand that the map is not an exact alternative to the real site amplification depending on frequency. Either way, the detail geophysical structure beneath a seismic station is a key for understanding the site amplification. For the 3-D basin model, the structure can constrain the number of possible models. For the interpolation, it is useful for verification and regression of the interpolation model as a sample. Many research works have addressed these issues by using data of vertical arrays (Seale & Archuleta 1989; Huang & Chiu 1996). Spectral ratio between records at the seismometers in the vertical array contains much information about the surface layers. It is compared to the synthetic spectral ratio by assuming material properties in the surface layers, and the properties are searched to fit it. The procedure has been applied for the estimation of the material properties in the surface layers.

In this paper, we focus on damping in surface layers at seismic stations. It is usually more difficult to estimate the damping than the other material properties of surface layers, such as *S*- and *P*-wave velocities (Kurita & Matsui 1997). Therefore, several special methods have been developed, and applied to the actual sites. Hauksson *et al.* (1987) obtained low quality factors Q in the near-surface layer using vertical array records in Baldwin Hills. Seale & Archuleta (1989) estimated the material damping coefficient by using the vertical array at McGee Creek, California. Aster & Shearer (1991) estimated mean quality factors based on the spectral ratio of the vertical arrays in the Southern California batholith region. Abercrombie (1997) estimated Q_P and Q_S in the Cajon Pass borehole in Southern California. Kurita & Matsui (1997) assessed the effect

 © The Authors 2013. Published by Oxford University Press on behalf of The Royal Astronomical Society.

of observation noises in estimating the soil properties via a sensitivity analysis. Yamada & Horike (2007) estimated Q values below 1 Hz in Osaka basin. Parolai *et al.* (2010) estimated the average Q_S by separating the contributions of upgoing and downgoing waves, and applied it to the vertical array in Istanbul, Turkey. Many related researches have also been reported in Japanese, for example, Takemura *et al.* (1993), Tsujihara & Sawada (2003) and Sato *et al.* (2006). All of the works have indicated low quality factors in the surface layers, $Q_S \approx 10$–50; however, we should take care of some results focusing on the amplitude decay due not only to the damping, but also the reflection and transmission on the layer interfaces.

The quality factor is originally defined by the energy loss per a cycle (e.g. Aki & Richards 2002), and many researches related to the attenuation model of the interior Earth (e.g. Tsumura *et al.* 1996, 2000; Eberhart-Phillips & Chadwick 2002; Pozgay *et al.* 2009) stand on the assumption that the energy loss due to the reflection can be evaluated as the attenuation due to scattering. To estimate the damping solely in the surface layer, one of the main problems is that all the wave energy do not arrive at the free surface passing through the layers even when the materials do not have the damping. This is because of the reflection at the material interfaces with a sharp contrast in velocity. Therefore, some forward simulations are required to eliminate the effect of reflection and transmission on the layer interfaces, as performed by Seale & Archuleta (1989), Kurita & Matsui (1997) and Yamada & Horike (2007).

Recently, Goto *et al.* (2011) discovered a conserved quantity in the surface layer, namely, normalized energy density (NED). The NED keeps a constant value independent of the material velocity and density even for the layers containing sharp velocity contrast, and can automatically eliminate the effect from reflection and transmission on the material interfaces. This property is similar to the energy conservation law, and thus, it may allow us to adopt a similar approach for estimating the attenuation model of the interior Earth. In this paper, we simulate the effect of the damping on the NED, and apply it to estimate the damping of the surface layers at Katagihara site in Japan.

2 NORMALIZED ENERGY DENSITY

A multilayered model consisting of n horizontal surface layers (#1-n) over a half-space basement (#0) is considered, as shown in Fig. 1. The S-wave velocity, the density, and the thickness of the kth layer are β_k, ρ_k and H_k, respectively. Materials of each layer and basement are linear elastic. When SH waves transmit vertically into the surface layers, through the interface between the nth layer and the basement, full 3-D wave equations are contracted in a 1-D wave equation. In the case, the NED for the kth layer is defined as follows (Goto *et al.* 2011):

$$\mathrm{NED}_k \equiv \lim_{\Omega \longrightarrow \infty} \frac{1}{\Omega} \int_0^{\Omega} \rho_k \beta_k \left| \frac{A_k(\omega)}{A_0(\omega)} \right|^2 \mathrm{d}\omega, \tag{1}$$

where A_0 is the Fourier amplitude of the incident wave that is the upgoing wave in the basement, and A_k is the Fourier amplitude of the upgoing wave in the kth layer. ω is the angular frequency. The integration is only applied to a positive value of ω, instead of the original definition (Goto *et al.* 2011), in which both the negative and positive values are integrated. This is permitted because the integrand is an even function when A_k/A_0 is causal.

The value is proved to be constant, $\mathrm{NED} = \rho_0\beta_0$, through the surface layers and the basement, analytically for the two-layered case and numerically when there are more than three layers (Goto

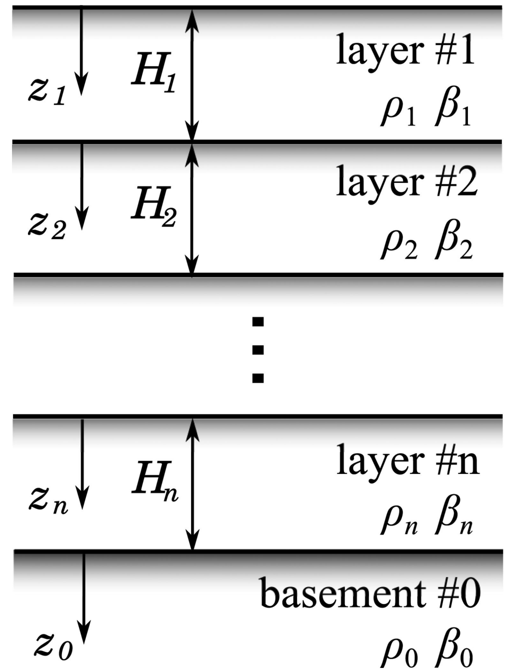

Figure 1. Multilayered model consisting of n layers over a half-space basement.

et al. 2011). This suggests that the NED is a conserved quantity through the layered structure and that it is evaluated without detailed physical properties when a ground transfer function ($2A_1/A_0$) and an impedance of the basement are available.

The NED conservation is confirmed when the materials have no dampings. Similar to the energy absorption, the NED may decrease depending on the damping. In the following section, we examine the dependence of the damping on the NED based on numerical simulations.

3 EFFECT OF DAMPING

3.1 Damping coefficient and apparent quality factor

In order to account for the effect of an damping on the NED in the uppermost layer, we introduce two different types of representations, (1) a complex stiffness and (2) the apparent quality factor. Note that we use an amplitude ratio of upgoing waves, A_1/A_0, from the basement to the free surface that is not the same as the spectral ratio between the ground motions recorded in a downhole vertical array. This is because the downhole records contain downgoing waves B_0 as well as upgoing waves. The spectral ratio between the records becomes $2A_1/(A_0 + B_0)$, which is different from the amplitude ratio A_1/A_0.

The complex stiffness is a conventional way to simulate a wave propagation considering the damping in the surface layers (e.g. Seale & Archuleta 1989; Kurita & Matsui 1997). Damping coefficient h is considered in an imaginary part of the stiffness:

$$\mu^* = \mu(1 + 2\mathrm{i}h), \tag{2}$$

where μ is the shear modulus defined by $\rho\beta^2$. i denotes an imaginary unit. The amplitude ratio A_1/A_0 is calculated from a propagation matrix (Haskell 1960) substituting the complex stiffness into the

Downloaded from http://gji.oxfordjournals.org/ at Kyoto University Library on July

material property. Quality factor Q_S is inversely proportional to the damping.

$$Q_S = \frac{1}{2h}. \tag{3}$$

This procedure allows us to set different values for Q_S in each layer, whereas the Q_S estimation requires the non-linear inversion scheme (Yamada & Horike 2007), for example, a genetic algorithm (Holland 1975).

The apparent quality factor is an alternative approach used to simply model the amplitude decay in the surface layers. Several researches have adopted a similar way to estimate the quality factor (e.g. Hauksson *et al.* 1987; Aster & Shearer 1991; Abercrombie 1997). For example, Abercrombie (1997) assumed the exponential attenuation model for the spectral ratio, and Parolai *et al.* (2010) assumed a similar exponential model for the amplitude ratio as

$$\frac{A_1(\omega)}{A_0(\omega)} = \frac{A_1(0)}{A_0(0)}\, \mathrm{e}^{-\omega T/2Q_{Sa}}, \tag{4}$$

where T denotes the one-way traveltime from the basement to the free surface. The model has allowed for the stable estimation of Q_{Sa} based on a regression analysis, although it cannot exclude the amplitude decay due to the reflection at the material interfaces. If the resonance is modelled by an amplitude ratio without the damping, another representation is available for separating the contribution from the damping and the resonance as follows:

$$\frac{A_1(\omega)}{A_0(\omega)} = \frac{A_1(\omega)^{\text{without damping}}}{A_0(\omega)}\, \mathrm{e}^{-\omega T/2Q_{Sa}}. \tag{5}$$

Since the representation does not give the same amplitude ratio as the method with complex stiffness, we refer to apparent quality factor to Q_{Sa} in order to distinguish it from Q_S by eq. (3).

For the two-layered case, the amplitude ratio evaluated from the complex stiffness is approximately represented as follows:

$$\frac{A_1(\omega)}{A_0(\omega)} = \frac{2\mathrm{e}^{-\omega h H_1/\beta_1}}{\left(\mathrm{e}^{\mathrm{i}\omega H_1/\beta_1} + \mathrm{e}^{-\mathrm{i}\omega H_1/\beta_1}\mathrm{e}^{-2\omega h H_1/\beta_1}\right) + \mathrm{i}R^*\left(\mathrm{e}^{\mathrm{i}\omega H_1/\beta_1} - \mathrm{e}^{-\mathrm{i}\omega H_1/\beta_1}\mathrm{e}^{-2\omega h H_1/\beta_1}\right)}, \tag{6}$$

where $(1 + 2\mathrm{i}h)^{1/2}$ is approximated by $1 + \mathrm{i}h$, assuming the damping coefficient is small enough. R^* denotes the complex impedance ratio between the surface layer and the basement that is $\rho_1\beta_1(1 + ih)/\rho_0\beta_0$. On the other hands, the amplitude ratio evaluated from the apparent quality factor via eq. (5) is

$$\frac{A_1(\omega)}{A_0(\omega)} = \frac{2\mathrm{e}^{-\omega H_1/2\beta_1 Q_{Sa}}}{\left(\mathrm{e}^{\mathrm{i}\omega H_1/\beta_1} + \mathrm{e}^{-\mathrm{i}\omega H_1/\beta_1}\right) + \mathrm{i}R\left(\mathrm{e}^{\mathrm{i}\omega H_1/\beta_1} - \mathrm{e}^{-\mathrm{i}\omega H_1/\beta_1}\right)}, \tag{7}$$

where R denotes the impedance ratio that is $\rho_1\beta_1/\rho_0\beta_0$. The representations are obviously different, while a similar relation to eq. (3) may be available when we focus on the numerator.

$$Q_{Sa} \approx \frac{1}{2h}. \tag{8}$$

Fig. 2 shows one of the examples of the amplitude ratios calculated from the complex stiffness (solid line) and from the apparent quality factor (dotted line) for the two-layered case, whose impedance ratio from the basement to the surface layer is $R = 0.275$ and whose ratio of the thickness to the S-wave velocity is 0.44. The damping coefficient, $h = 0.02$, and the corresponding apparent quality factor, $Q_{Sa} = 25$, satisfy the relation in eq. (8). The amplitude ratios are similar with frequencies lower than 1 Hz, whereas

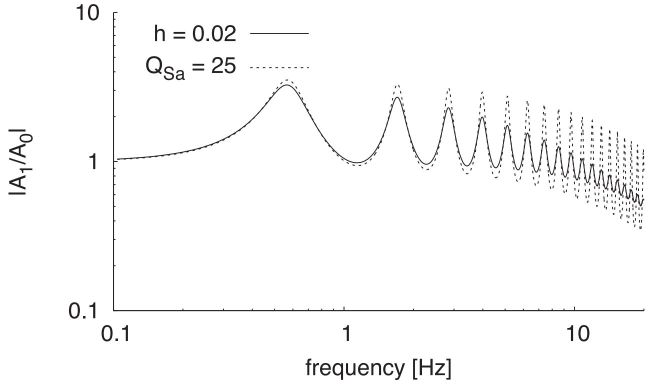

Figure 2. Comparison of the amplitude ratios calculated by the complex stiffness, $h = 0.02$, and the apparent quality factor, $Q_{Sa} = 25$, on the free surface ($R = 0.275$ and $H_1/\beta_1 = 0.440$).

ripples for the apparent quality factor do not decrease with frequencies higher than 1 Hz. On the other hand, it averagely decays with a similar gradient.

3.2 Effect on NED

The NED is defined by the average up to the positive infinity frequency (eq. 1); however, the definition is not appropriate for the real case that a seismometer has a particular support frequency bands. Also, the amplitude ratio incorporating the damping decays in high frequencies. To evaluate the value of the NED, we take the average in a finite frequency range, truncating the higher and lower frequency components as follows:

$$\mathrm{NED}_1 = \frac{1}{2\pi(f_2 - f_1)} \int_{2\pi f_1}^{2\pi f_2} \rho_1\beta_1 \left|\frac{A_1(\omega)}{A_0(\omega)}\right|^2 \mathrm{d}\omega, \tag{9}$$

where f_1 and f_2 are the lowest and highest frequency supports in the analysis. In the following simulations, we adopt $f_1 = 0.1$ Hz and $f_2 = 20$ Hz, respectively.

The effect of the damping is examined by performing a Monte Carlo simulation for two- and six-layered cases. Three thousand models are randomly generated by sampling each physical value of the surface layers and the basement from uniform distributions within the range of 50–1000 m s^{-1} for the S-wave velocity and 1400–2400 kg m^{-3} for the density. In each model, the total thickness of the layers is determined by sampling a value from the uniform distribution within the range of 100–1000 m. For the six-layered case, four values are sampled from the uniform distribution within 0.0–1.0, and sorted in ascending order. The depth to each interfaces are determined by multiplying the total thickness and the four values. This procedure ensures the random thickness of each layer, and also controls the total thickness within 100–1000 m.

For each sample, four types of the damping coefficients, $h = 0$ (no damping), 0.005, 0.02 and 0.05, are simulated by using the complex stiffness. In addition, three types of the apparent quality factors, $Q_{Sa} = 100$, 25 and 10, are simulated by eq. (5). The damping is considered only in the surface layers, and the values are constant over the layers even for the six-layered case.

Figs 3 and 4 show the effect of the dampings on the NED for the two- and six-layered cases, respectively. The horizontal axis is the ratio of NEDs ($\mathrm{NED}_1/\mathrm{NED}_0$), which should be equal to 1 for the no damping cases if the original infinite integration is applied. The vertical axis is the number of samples. The results for the three types of apparent quality factors are plotted together in

Downloaded from http://gji.oxfordjournals.org/ at Kyoto University Library on July 17, 2013

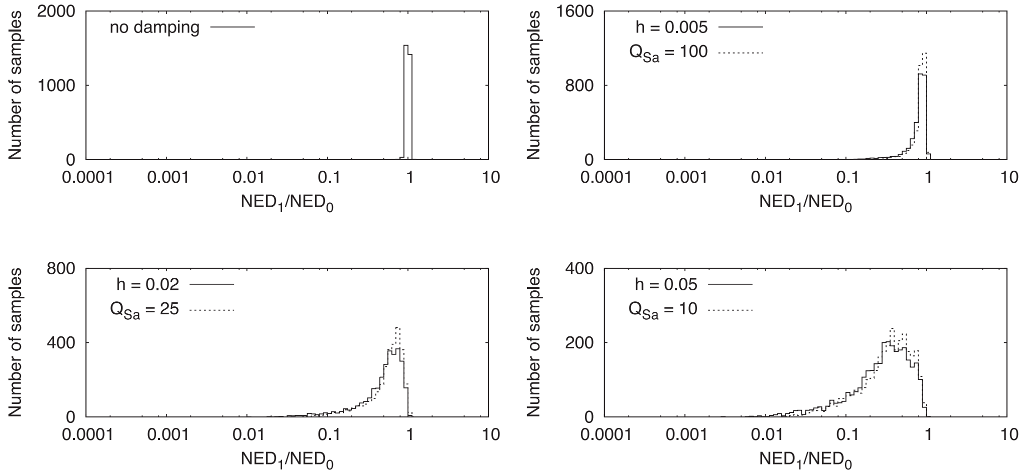

Figure 3. Comparison of the effect of the damping simulated by the complex stiffness and the apparent quality factor for two-layered case.

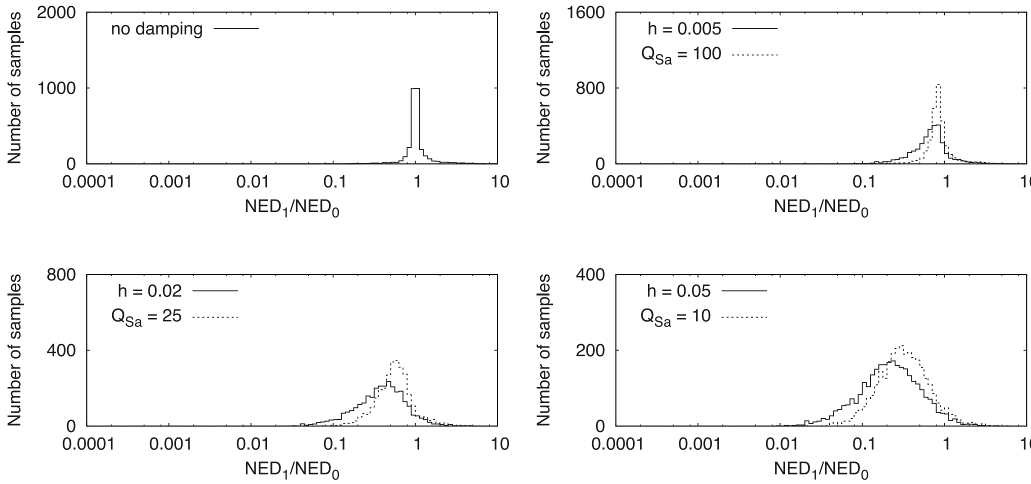

Figure 4. Comparison of the effect of the damping simulated by the complex stiffness and the apparent quality factor for six-layered case.

the corresponding cases for the damping coefficient in the relation given in eq. (8). For the no damping cases, samples for both the two- and six-layered cases are distributed around 1 in the NED ratio. In the original definition of NED, all samples should be 1, whereas variations are observed due to averaging in the finite frequency range, especially for the six-layered case. However, the variations are not major compared to the effect of the damping.

The mean values of the NED ratio decrease, and the variations increase as the damping increases. The results simulated from the apparent quality factor are similar to those from the complex stiffness for the two-layered case, whereas some discrepancies are observed between the distributions for the six-layered cases. The differences are not surprising because the definition is obviously different, while the similarity in terms of the effect on the NED is interesting for the two-layered cases. This implies that the apparent quality factor shows a similar property of the effect on the NED to the complex stiffness when the layered structure is simply modelled by two layers; for example, a sharp velocity contrast is expected between the surface layers and the basement, although generally it is not observed.

3.3 Total damping of surface layers

Attenuation models for the interior Earth, such as the crust structure, the subduction zone, etc., have been determined by many researchers (e.g. Tsumura *et al.* 1996, 2000; Eberhart-Phillips & Chadwick 2002; Pozgay *et al.* 2009). The attenuation is usually modelled by the decay of amplitude spectra $A(f)$, for example,

$$A(f) = S(f)\mathrm{e}^{-\pi f t^*}, \tag{10}$$

where $S(f)$ is a source model that usually follows the ω^2 model (Eberhart-Phillips & Chadwick 2002). f denotes a frequency. t^* is a measurable parameter accounting for the whole path attenuation defined as follows:

$$t^* = \int_{\text{ray path}} \frac{\mathrm{d}x}{c(x)Q(x)}, \tag{11}$$

where c is a material velocity corresponding waves. t^* originally comes from the energy decay along the ray tube, whereas t^* also accounts for also the effects of dispersion.

t^* in the surface layers was discussed in Aster & Shearer (1991). As they mentioned in their article, t^* includes the contribution of scatterings due to lateral inhomogeneities. Because the energy is not conserved through the layers, the relation between the amplitude ratio and the damping has not been discussed.

Fortunately, we have another conserved quantity NED; it deceases depending on the magnitude of the damping. The effect of the damping in terms of t^* should be examined. We introduce a total

Downloaded from http://gji.oxfordjournals.org/ at Kyoto University Library on July

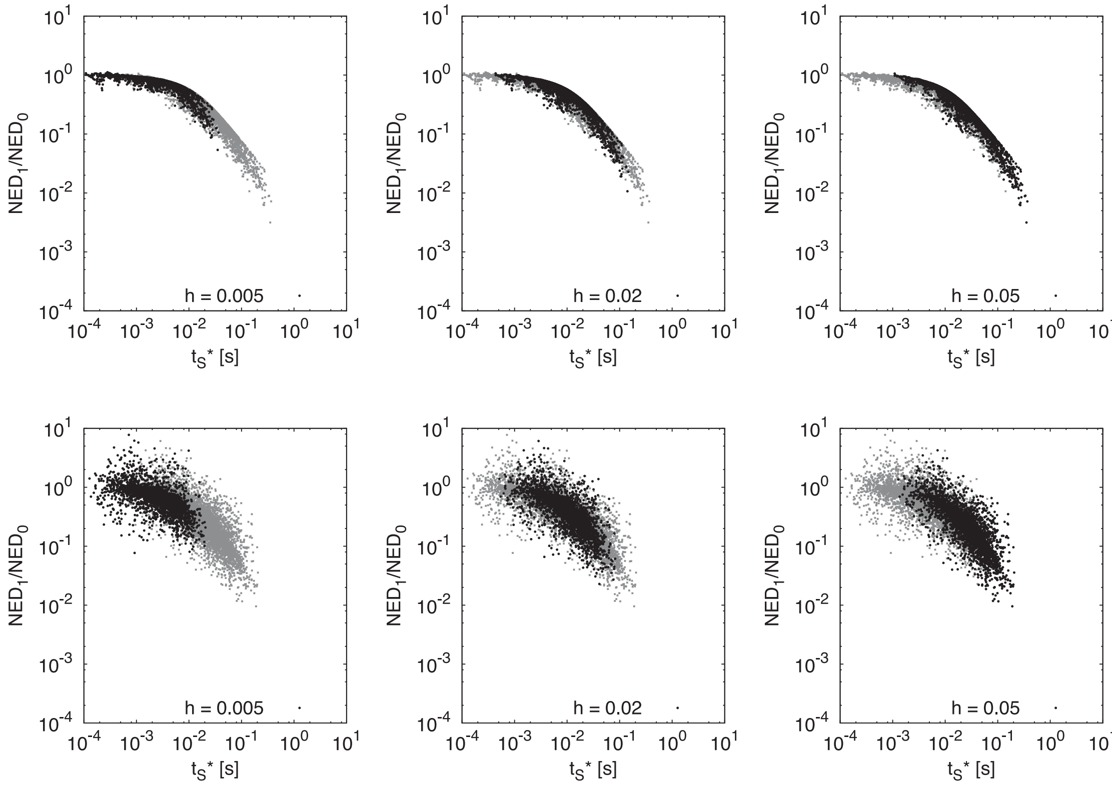

Figure 5. Effect of t_S^* for two-layered case (top panel) and the six-layered case (bottom panel). The gray points are the results of the other damping coefficients.

damping t_S^* to quantify the total contribution of the damping for the surface layers as follows:

$$t_S^* = \sum_{k=1}^{n} \frac{2H_k h_k}{\beta_k}. \tag{12}$$

The representation is compatible with the original definition of t^* in eq. (11), in which the total damping only accounts for the internal damping theoretically.

Fig. 5 shows the effect of the t_S^* on the NED ratio for the same two- and six-layered cases. Each sample shows the simulated results evaluated from the previous Monte Carlo simulations by using the complex stiffness (Figs 3 and 4): three thousand sets per each damping coefficient, $h = 0.005$, 0.02 and 0.05. The horizontal axis is the t_S^* evaluated from the definition in eq. (12), and the vertical axis is the NED ratio ($\mathrm{NED}_1/\mathrm{NED}_0$) that is the same as the horizontal axis in Figs 3 and 4. The results for each damping coefficient case are overlapped on those of the other cases; for example, the results for $h = 0.005$ are overlapped on the results for $h =$ 0.02 and 0.05 cases. The NED ratio clearly correlates to t_S^*, and the relation is independent of the values for the dampings. The correlation for the six-layered case is less than that for the two-layered case, whereas the correlation curve is almost similar in both cases.

To highlight the independence of the damping, we generate ten thousand sets of six-layered models with a randomly generated damping coefficient in each layer. The *S*-wave velocity, the density, and the thickness of each layer are randomly generated in the same range as that of the previous simulation, and the damping coefficient h is sampled from the uniform distribution within the range of 0–0.05. Note that the generated layered models have different values for the damping coefficient in each layer. Fig. 6 shows the effect of the t_S^* on the NED ratio. The samples also exhibit a clear

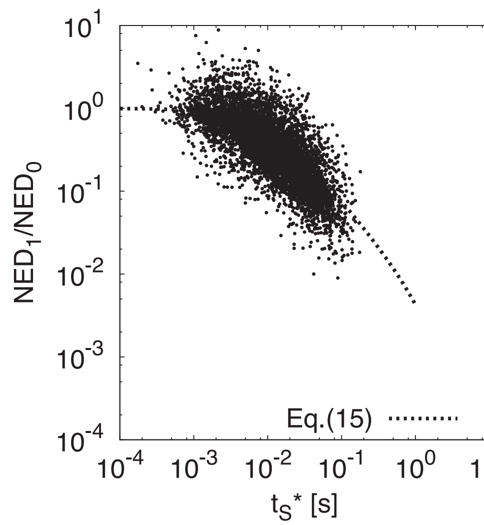

Figure 6. Effect of t_S^* for six-layered case with a variable damping coefficient. The dashed line represents the relation in eq. (15).

correlation between t_S^* and the NED ratio. This suggests that the direct estimation of total damping t_S^* is available based on the NED ratio.

The dependence is explained by a specific case of the apparent quality factor. For the two-layered case, when the impedance of the surface layer is equal to that of the basement ($R = 1$), the amplitude ratio A_1/A_0 is calculated from the apparent quality factor via eq. (7) as

$$\frac{A_1(\omega)}{A_0(\omega)} = \mathrm{e}^{-\mathrm{i}\omega H_1/\beta_1} \mathrm{e}^{-\omega H_1/2\beta_1 Q_{Sa}}. \tag{13}$$

Downloaded from http://gji.oxfordjournals.org/ at Kyoto University Library on July 17, 2013

In the above case, the NED ratio is analytically evaluated as follows:

$$\frac{\mathrm{NED}_1}{\mathrm{NED}_0} = \frac{Q_{Sa}/T}{2\pi(f_2 - f_1)}\left(\mathrm{e}^{-2\pi f_1 T/Q_{Sa}} - \mathrm{e}^{-2\pi f_2 T/Q_{Sa}}\right). \tag{14}$$

As shown in Fig. 3, because the effect on the NED ratio calculated from the apparent quality factor is similar that from the complex stiffness for the two-layered case, we can assume the relation of eq. (8). Under this assumption, t_S^* equals to T/Q_{Sa}. This suggests the direct relation between the t_S^* and the NED ratio, as follows:

$$\frac{\mathrm{NED}_1}{\mathrm{NED}_0} = \frac{1}{2\pi(f_2 - f_1)t_S^*}(\mathrm{e}^{-2\pi f_1 t_S^*} - \mathrm{e}^{-2\pi f_2 t_S^*}). \tag{15}$$

The relation is accepted only for specific cases, and it is also one of the available models. Fig. 6 also plots the relation of eq. (15). The curve passes through the group of the samples.

NED is evaluated from the amplitude ratio and the material impedance, as defined in eq. (9). This suggests that the NED ratio can be evaluated from only two pieces of information: (1) the impedance ratio between the uppermost layer and the basement and (2) the spectral ratio between the free surface response and the incident ground motion at the basement. Actual material parameters in the intermediate layers, such as the density, the *S*-wave velocity, and the thickness of the layer, are not explicitly required. No information is required when we can directly observe the spectral ratio. For the downhole vertical arrays, the borehole records at the basement consist of both the upgoing and downgoing waves, and the spectral ratio between the records on the free surface and the basement does not become the amplitude ratio that we want to obtain. One of the direct approaches is to take the spectral ratio between the records at nearby stations on both free surfaces; (1) at the deposit site and (2) at the bedrock site. When the incident wave at the deposit site is assumed to be the same as the incident wave at the bedrock site, the spectral ratio becomes A_1/A_0. This allows the direct estimation of the total damping without the information on the intermediate layers.

3.4 Frequency-dependent damping

Some researches have pointed out that the quality factor depends on frequency even in the near-surface layers (e.g. Kudo & Shima 1970; Kobayashi *et al.* 1992; Satoh *et al.* 1995). The major mechanism caused the frequency dependence is usually explained by the scattering attenuation due to the irregular interfaces and/or material inhomogenety. In the previous discussion, we assume that the damping coefficient and the quality factor are independent of frequency, whereas it may not be realistic. We perform an additional numerical simulation considering frequency-dependent damping, and discuss the results compared to the previous ones.

Frequency-dependent quality factor has been modelled by a function form of $Q_S = Q_{S0} f^{\alpha}$, where Q_{S0} is a coefficient depending on the *S*-wave velocity and/or soil classifications. α takes a value almost in the range from 0.0 to 1.0, which have been estimated from the observed ground motions (e.g. Satoh *et al.* 1995). A variety of established models is well summarized in Fukushima & Midorikawa (1994). Recently, Yamada & Horike (2007) suggested a model of the frequency-dependent quality factor proportional to a negative power of frequency in the low-frequency region, and Sato *et al.* (2006) proposed lower limit of Q^{-1} in the high-frequency region. Although both recent models are interesting options, we adopt the conventional frequency-dependent model, $0.0 < \alpha < 1.0$, in order to clarify the effect of frequency dependence.

We generate 10 000 sets of six-layered models with a randomly generated damping coefficient depending on frequency. The values of the *S*-wave velocity, the density, and the thickness of each layer are randomly sampled from the same range as that of the previous simulation. The frequency-dependent damping coefficient is modelled by $h = h_0 f^{-\alpha}$, where h_0 corresponds to Q_{S0} $(=1/2h_0)$. h_0 and α are sampled from the uniform distribution within 0–0.05 and 0–1, respectively. The frequency-dependent models in each layer, such as h_0 and α, are different each other.

The total damping t_S^* cannot be directly defined under the frequency-dependent model because the value depends on the frequency. We alternatively define $\bar{t_S^*}$, an averaged value of the total damping, by taking the frequency average, as follows:

$$\begin{aligned}\bar{t_S^*} &= \frac{1}{f_2 - f_1}\int_{f_1}^{f_2}\sum_{k=1}^{n}\frac{2H_k h_k(f)}{\beta_k}\,\mathrm{d}f \\ &= \begin{cases}\sum_{k=1}^{n}\frac{2H_k h_{0k}}{\beta_k} & \text{for } \alpha_k = 0 \\ \sum_{k=1}^{n}\frac{2H_k h_{0k}}{\beta_k}\frac{f_2^{1-\alpha_k} - f_1^{1-\alpha_k}}{(1-\alpha_k)(f_2 - f_1)} & \text{for } \alpha_k > 0\end{cases},\end{aligned} \tag{16}$$

where h_{0k} and α_k denote the values in kth layer. The averaged value $\bar{t_S^*}$ is equivalent to the total damping t_S^* when all the dampings are independent of frequency.

Fig. 7 shows the relation between the averaged value $\bar{t_S^*}$ and the NED ratio on the ten thousand samples. It also exhibits a clear correlation between them, which is similar to the correlation between the total damping t_S^* and the NED ratio in the case of frequency-constant dampings as shown in Fig. 6. We also plot the relation of eq. (15), substituting $\bar{t_S^*}$ instead of t_S^*, in Fig. 7. The curve passes through the group of the samples. This implies that the total damping directly estimated from the NED ratio corresponds to the frequency averaged value $\bar{t_S^*}$. In other words, when the total damping is defined by the frequency average, its direct estimation from the NED ratio is valid whether the damping depends on frequency or not. In the following discussion, we focus on the frequency-independent damping, whereas this suggests that the estimated total damping is regarded as its frequency average for the case of frequency-dependent damping.

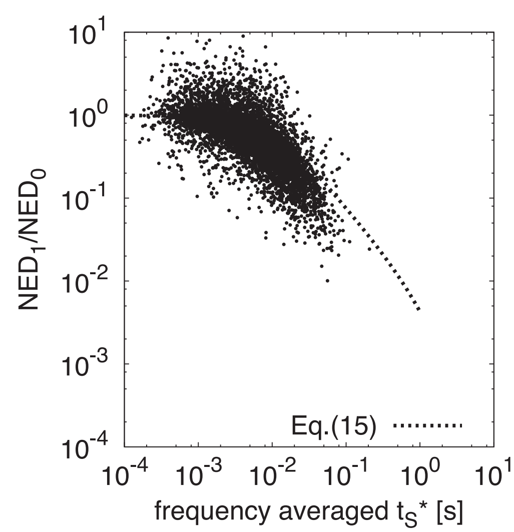

Figure 7. Averaged $\bar{t_S^*}$ for six-layered case with frequency-dependent quality factor. The dashed line represents the relation in eq. (15).

Downloaded from http://gji.oxfordjournals.org/ at Kyoto University Library on July

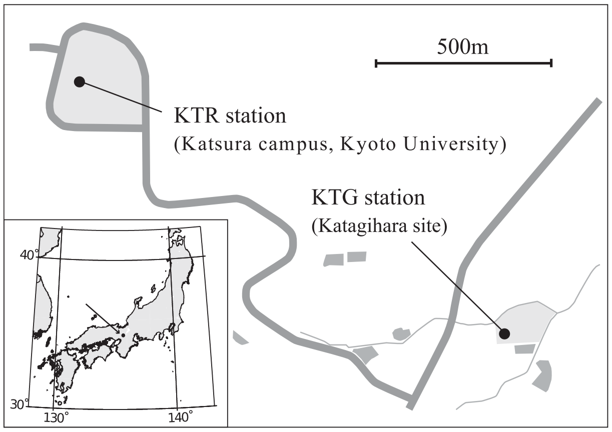

Figure 8. Location of KTR at the Katsura Campus of Kyoto University and KTG at the Katagihara site.

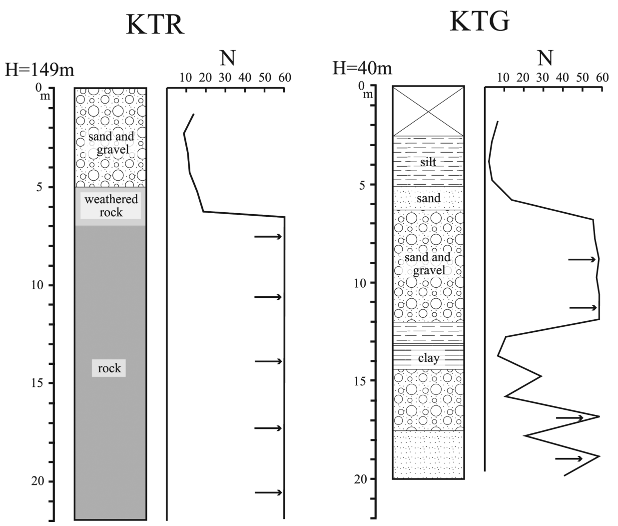

Figure 9. Borehole data and SPT-N values in about 20 m of depth at KTR and KTG sites.

4 TOTAL DAMPING AT KATAGIHARA SITE

4.1 Seismic stations KTG and KTR

We focus on the Katagihara site located in Kyoto, Japan. Local damage was observed in the area during the 1995 Kobe earthquake even about 70 km away from the epicentre (Kansai Geo-informatics Network 2002). The Katsura Campus of Kyoto University is located just 1 km away in a northwestern direction from the Katagihara site, as shown in Fig. 8. The elevation at the Katagihara site is about 40 m, while it increases to 150 m at the Katsura Campus, and an outcrop of bedrock is observed at the Katsura Campus. The geology and geography suggest that the Katagihara fault is located in between the sites, for example, Uemura (1990), and that a deep and soft alluvial deposit overlies Palaeozoic rock, for example, Iwano *et al.* (2001).

Seismic stations for observing strong ground motions have been installed at both sites, namely, KTG at the Katagihara site (N 34.973°, E 135.693°) and KTR at the Katsura Campus (N 34.983°, E 135.677°). The stations belong to the seismic network organized by the Committee of Earthquake Observation and Research in the Kansai Area (CEORKA) (Kagawa *et al.* 2004b), in operation since 1996 for KTG site and since 2009 for KTR site. Each station consists of three servo-velocity types of sensors, which supports a flat response in wide frequency range, 0.01–100 Hz in –3 dB. The A/D sampling rate is 100 Hz. Fig. 9 shows the borehole data and the SPT-N values at a depth of about 20 m. A rock layer appears at 6 m at KTR site, while sand and gravel layers continue to 20 m at KTG site. Soft clay with a low N value of about 10 appears at 15 m at KTG site. This also indicates a soft deposit at the Katagihara site relative to the Katsura Campus. On the other hand, KTR site is supposed to be the rock site because a seismometer is settled on the stiff foundation constructed just above the bedrock and the foundation is separated from the foundation of the building.

We assume that the rock at KTR site has the same material properties as the basement beneath the Katagihara site, and that the incident waves are common for both KTR and KTG sites. Under these assumptions, the spectral ratio of the records at KTG and KTR sites becomes the amplitude ratio between the upgoing waves in the uppermost layer and the basement at KTG site. This allows the direct evaluation of the NED ratio directly from the spectral ratio.

Local earthquakes of the epicentre distances within 150 km have been selected from the available records from 2009 to 2010. The detailed source parameters are listed in Table 1, and the epicentre locations of nine events are plotted on the map in Fig. 10. Eight events (1–7 and 9) are distributed in the western direction of the sites with an epicentre distance of about 15 km, and the other event (8) is located in the southern direction with an epicentre distance of about 80 km. Fig. 11 shows the observed velocity waveforms at the KTG and KTR sites in both horizontal components, east to west (EW) and north to south (NS), for events 2 and 8 in Table 1. The amplification at the KTG site has a peak value of about 2.5, and increase of the duration is clearly observed. This also indicates that the site amplification due to the surface layers should be considered at the KTG site.

Spectral ratios in each component for each of the nine events are calculated. The Fourier amplitude of each velocity waveform

Table 1. Parameters of the selected nine earthquakes.

Date	Time (hh:dd JST)	Latitude[a] (N deg)	Longitude[a] (E deg)	Depth[a] (km)	M_{JMA}[a]
1. 2009 September 19	01:46	35.097	135.562	12	3.6
2. 2009 October 25	05:50	35.088	135.571	13	3.9
3. 2009 November 9	21:59	35.057	135.613	12	3.0
4. 2009 November 18	13:13	34.942	135.540	9	3.4
5. 2009 December 31	18:03	35.017	135.558	14	3.0
6. 2010 January 21	04:18	34.960	135.445	11	3.7
7. 2010 February 16	07:33	34.918	135.570	11	3.6
8. 2010 July 21	06:19	34.205	135.693	58	5.1
9. 2010 August 13	21:10	35.017	135.557	14	2.8

[a]After JMA.

Downloaded from http://gji.oxfordjournals.org/ at Kyoto University Library on July 17, 2013

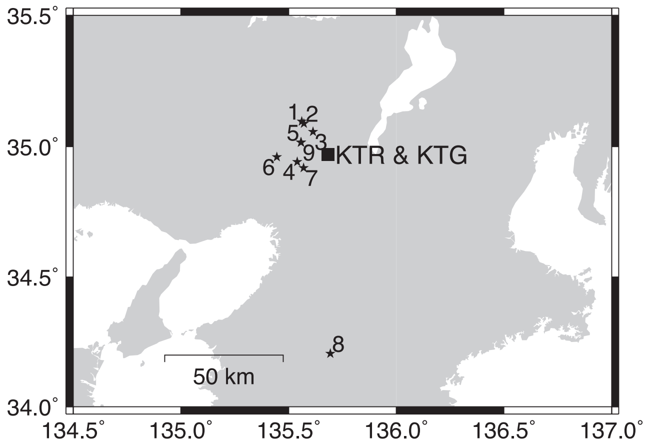

Figure 10. Location of the epicentres for the selected nine earthquakes (detailed in Table 1).

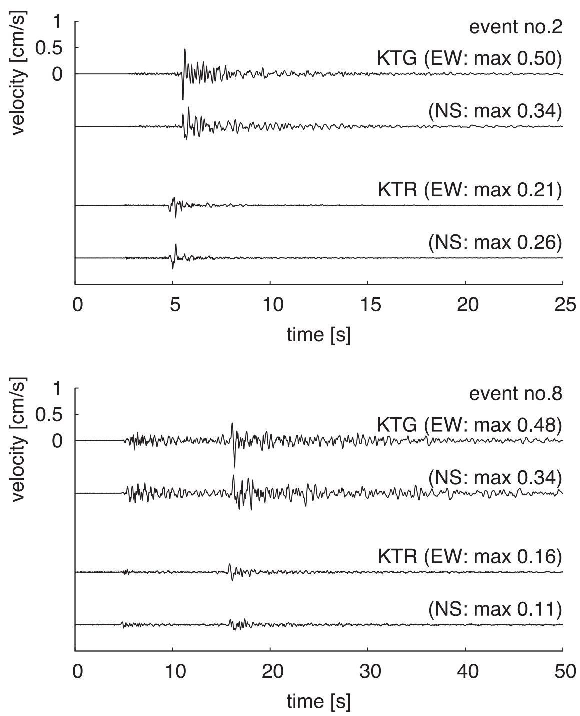

Figure 11. Velocity waveforms at KTG and KTR sites for event no. 2 (top panel) and no. 8 (bottom panel).

is smoothed by a Parzen window with a width of 0.1 Hz, and the one for KTG site is divided by the one for KTR site. Fig. 12 shows the spectral ratios in the horizontal components plotted by dashed lines for each spectral ratio, and a solid line for the average of the spectral ratios. The peaks are observed at around 0.5 and 6.0 Hz, and the average exceeds 1 in the wide frequency range, 0.2–10 Hz.

4.2 Estimation of dampings by conventional method

We first apply a conventional method to estimate the dampings in each layer at the KTG site. The synthetic spectral ratio is calculated from the complex stiffness under the given material properties, such as the *S*-wave velocity, the density, the layer thickness, and the damping coefficient. This is because *S*-wave velocity and density structures are not available at the KTG site, and there is no direct information how deep the soft deposit continues over 20 m. The

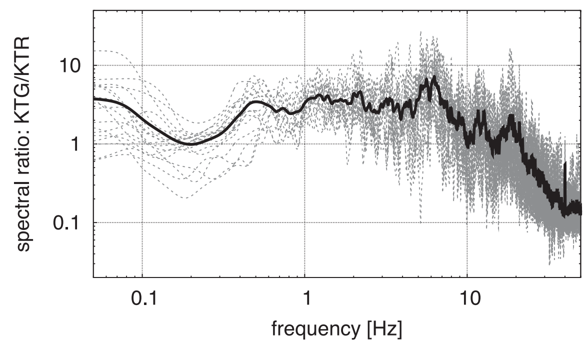

Figure 12. Spectral ratio of KTG/KTR for each earthquake (dash lines) and the average (solid line).

synthetic one is compared to the averaged spectral ratio of the observation, as shown in Fig. 12, and the optimum model is searched based on the discrepancy between the synthetic and observed spectral ratios via a non-linear inversion scheme, for example, Kurita & Matsui (1997) and Yamada & Horike (2007). A six-layered model with a five surface layers and a half-space basement is assumed. The layer thickness shallower than 20 m is based on the borehole data (Fig. 9). Prior to applying the inversion scheme, the *S*-wave velocity, the density, and the damping coefficient models are manually modified to fit the observed spectral ratio.

The optimum parameter sets are searched using a simple genetic algorithm (Holland 1975); 100 populations, 200 generations, 0.5 per cent mutation probability and 75 per cent crossover probability. The search ranges of each parameter are limited to within 50–200 per cent of the initial values for the *S*-wave velocity, the density, and the layer thickness, and within 0–0.1 for the damping coefficient. The synthetic spectral ratio is calculated from the propagation matrix (Haskell 1960) substituting the complex stiffness into the material properties. The objective function is defined as follows:

$$J(\boldsymbol{m}) = \frac{\langle |O(\boldsymbol{m}) - S(\boldsymbol{m})|^2 \rangle}{\langle |O(\boldsymbol{m})| \rangle \langle |S(\boldsymbol{m})| \rangle} \longrightarrow \min, \tag{17}$$

where $\boldsymbol{m}$ is an estimation vector whose component consists of the *S*-wave velocity, the density, the layer thickness, and the damping. $O(\boldsymbol{m})$ and $S(\boldsymbol{m})$ denote the observed and synthetic spectral ratios, and the brackets $\langle\,\rangle$ means the following integration operator in frequency, for example,

$$\langle |O(\boldsymbol{m})| \rangle = \int_{f_1}^{f_2} \frac{|O(\boldsymbol{m}, f)|}{f} \, \mathrm{d}f, \tag{18}$$

$$\langle |O(\boldsymbol{m}) - S(\boldsymbol{m})|^2 \rangle = \int_{f_1}^{f_2} \frac{|O(\boldsymbol{m}, f) - S(\boldsymbol{m}, f)|^2}{f} \, \mathrm{d}f, \tag{19}$$

where f_1 and f_2 are the low and high cut-off frequencies. In this case, we set $f_1 = 0.1$ Hz and $f_2 = 20$ Hz to be consistent with the definition of NED. The integrand is inversely proportional to the frequency. This is consistent with the integration by the log-scaled frequency, and it emphasizes the low frequency components in quantifying the discrepancy between the observed and synthetic spectral ratios.

We perform ten trials, changing the set of random numbers and starting from the same initial model, and obtain ten independent optimum layered models. Fig. 13 shows a comparison of the observed and the synthetic spectral ratios for the 10 optimum models. The synthetic ones agree well with the observed ones, and they converge to similar shapes. The peak values and the corresponding frequencies, 0.5 and 6.0 Hz, are simulated well. Fig. 14 shows the optimum velocity models and the damping models. The dashed lines indicate

Downloaded from http://gji.oxfordjournals.org/ at Kyoto University Library on July [redacted]

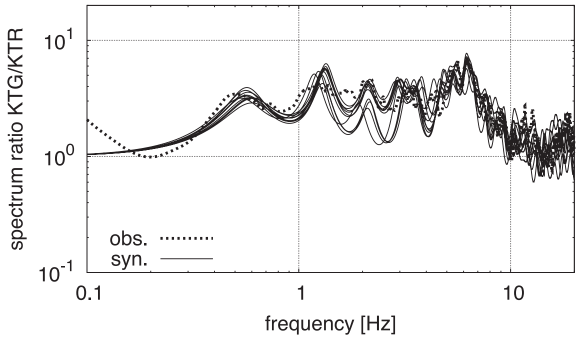

Figure 13. Comparison of the synthetic and observed spectral ratios for KTG/KTR.

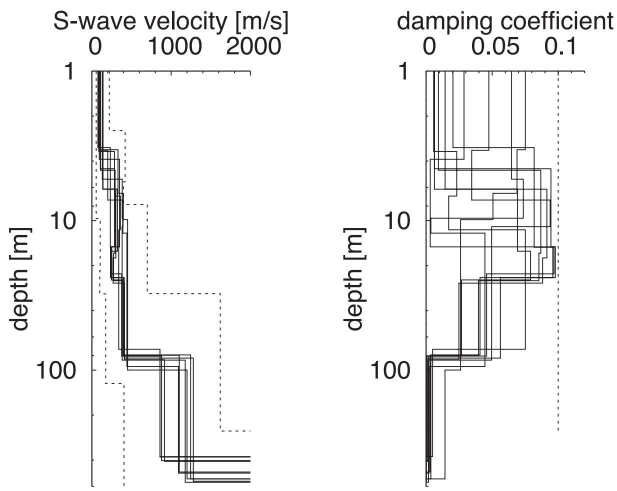

Figure 14. Optimum velocity and damping models evaluated by the genetic algorithm. The dashed lines denote the search range.

the search range during the non-linear inversion scheme. The velocity models converges well among the ten independent simulations; however, there is much variation among the damping models. Thus, the models evaluated from the ten simulation cases converge to the optimum model, but this is not the case for the damping model. The search range of the damping coefficient, 0–0.1, that corresponds to $Q_S = 5 \sim \infty$, is wide enough to model the dampings of the surface layers based on the previous works. This implies that the damping coefficients in each layer are less sensitive to the spectral ratio, which has been reported in several studies (Kurita & Matsui 1997; Tsujihara & Sawada 2003). Therefore, some average quantities are required to quantify the damping, such as the average quality factor (Parolai *et al.* 2010), etc.

4.3 Estimation of total damping t_S^*

We estimate the total damping t_S^* at the KTG site based on the relation between t_S^* and the NED ratio. The parameter ranges are adjusted to generate the appropriate random models at KTG site. Because the *S*-wave velocity in the surface layer can be assumed to be less than that of the basement, as seen in the amplification and the duration of the observed ground motions, the ranges in *S*-wave velocity are 50–2000 m s^{-1} for the surface layers and 700–3200 m s^{-1} for the basement. The density and the total thickness of the layer are generated from the ranges 1400–2400 kg m^{-3} and 100–1000 m. The damping coefficients are in the range of 0–0.1. Note

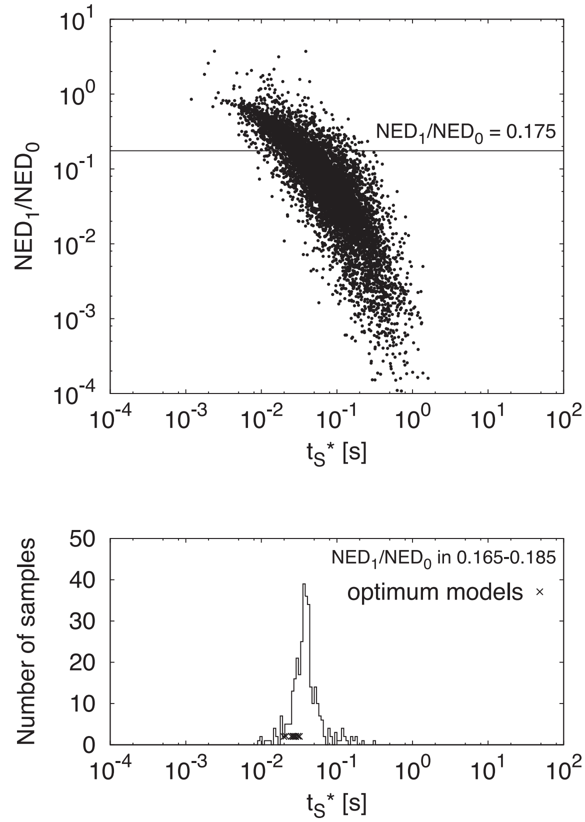

Figure 15. Simulation results for ten thousand random models for evaluating the relation between the NED ratio and t_S^* (top panel), and the histogram of the samples corresponding to 0.165–0.185 of the NED ratio (bottom panel).

that the simulation ranges are different from those in the previous section (Fig. 6).

The 10 000 random layered models are generated numerically, and the relation between t_S^* and the NED ratio is plotted in Fig. 15. As discussed in the previous section, the NED ratio correlates well with the total damping t_S^*.

To evaluate the NED ratio directly, the spectral ratio between the records at KGT and the records at KTR site, and also the impedances of the uppermost layer at each site are required. The spectral ratios are available from the observed records, whereas the impedance ratio is not available at this time. A technique to measure the impedances should be developed. Note, however, that the measurement is only for the uppermost layers, not for all of the properties at the sites. We human, as well as any equipment, can touch or come into contact with the material without disturbing the ground itself, such as occurs in drilling for boreholes. In this paper, we demonstrate the estimation of the total damping by assuming that the impedance ratio is available. Here, we give the impedance of the uppermost layer at KTG and KTR sites as the average of the ten optimum values obtained using the conventional method. Then, the NED ratio is directly calculated from the integration of eq. (9) as 0.175.

Fig. 15 also shows the line 0.175 of the NED ratio. The line cuts the group of samples in the range of about $t_S^* = 0.01$–0.2. The histogram of the samples within the range of 0.165–0.185 of the NED ratio is shown in the bottom panel of Fig. 15, and it suggests that most samples are distributed around $t_S^* = 0.038$. As the distribution shape depends on the random generation of the model, the variation does not have much physical meanings. If we

Downloaded from http://gji.oxfordjournals.org/ at Kyoto University Library on July 17, 2013

consider the total damping as the value corresponding to the sample peak, the estimated value of t_S^* by using the NED ratio is 0.038 at KTG site.

To verify the estimated t_S^* value, we compare the total dampings calculated from the ten optimum models evaluated from the conventional method. The results from the optimum models are plotted together in the histogram in Fig. 15, and they are distributed within the range of 0.020–0.032. The large variation for the optimum models is not seen in terms of the total damping coefficients, and the value estimated directly from the NED ratio ($t_S^* = 0.038$) is close to the values for the optimum models. This suggests that total damping t_S^* is one of the stable variables for quantifying the damping property in the near-surface layer, and that the value can be directly evaluated from the NED ratios.

5 CONCLUSION

We have proposed a direct estimation method of the total damping in the surface layers based on the NED. The NED ratio, defined as the NED for the uppermost layer divided by the NED for the basement, was found to correlate well with the total damping t_S^*. We have examined its applicability to an actual site using the spectral ratio between the deposit site KTG and the bedrock site KTR. The total damping in the surface layers at the KTG site was estimated at 0.038 directly from the value of NED ratio. The value was seen to be similar to those estimated via a conventional method using the non-linear inversion scheme.

Attenuation parameter t^* for the Earth interior model is not a material-specific parameter because t^* depends on the ray path. Therefore, the attenuation model for the Earth interior was quantified by a quality factor, eliminating the contribution of the ray path. On the other hand, total damping in the surface layers, t_S^*, is a specific parameter at the site. The one-way traveltime, T, from the basement to the free surface, may turn the total damping into the average quality factor, T/t_S^*, in which T is also a site-specific parameter. This property is an important point to note in the total damping.

A simulated group of samples, representing the relation between the NED ratio and the total damping (Figs 6 and 15) is independent of the sites. The samples can be applied to any other sites if the material properties are expected to lie in the range of the random simulation. This is the benefit that no simulations are required in order to apply it to the other sites when it has already been prepared.

In this paper, we have demonstrated a performance whereby we obtain the impedance at the uppermost layers at KTG and KTR sites. The measurement technique and analysis method must be further developed in the near future. If the technique is readily available, the total damping can be quantified at the site using only the records on the free surface and without detailed velocity and density models for beneath the site.

ACKNOWLEDGEMENTS

We thank Professor Tomotaka Iwata, Professor Yoshikazu Takahashi, Dr Kimiyuki Asano, Dr Takahiko Uchide, Dr Saeko Kita and many related researchers for their beneficial discussions. We are grateful for the use of the ground motion records organized by the Committee of Earthquake Observation and Research in the Kansai Area.

REFERENCES

Abercrombie, R.E., 1997. Near-surface attenuation and site effects from comparison of surface and deep borehole recordings, *Bull. seism. Soc. Am.,* **87,** 731–744.

Aki, K. & Richards, P.G., 2002. *Quantitative Seismology,* 2nd edn, University Science Books, Sausalito, CA.

Aster, R.C. & Shearer, P.M., 1991. High-frequency borehole seismograms recorded in the San Jacinto fault zone, Southern California, Part 2. Attenuation and site effects, *Bull. seism. Soc. Am.,* **81,** 1081–1100.

Borcherdt, R.D., 1970. Effects of local geology on ground motion near San Francisco bay, *Bull. seism. Soc. Am.,* **60,** 29–61.

Eberhart-Phillips, D. & Chadwick, M., 2002. Three-dimensional attenuation model of the shallow Hikurangi subduction zone in the Raukumara Peninsula, New Zealand, *J. geophys. Res.,* **107**(B2), ESE 3-1–ESE 3-15.

Fukushima, Y. & Midorikawa, S., 1994. Evaluation of site amplification factors based on average characteristics of frequency dependent Q^{-1} of sedimentary strata, *J. Struct. Constr. Eng. AIJ,* **460,** 37–46 (in Japanese with English abstract).

Goto, H., Sawada, S., Morikawa, H., Kiku, H. & Ozalaybey, S., 2005. Modeling of 3D subsurface structure and numerical simulation of strong ground motion in the Adapazari basin during the 1999 Kocaeli earthquake, Turkey, *Bull. seism. Soc. Am.,* **95,** 2197–2215.

Goto, H., Sawada, S. & Hirai, T., 2011. Conserved quantity of elastic waves in multi-layered media: 2D SH case—normalized energy density, *Wave Motion,* **48,** 602–612.

Goto, H. *et al.*, 2012. Very dense seismic array observations in Furukawa district, Japan, *Seism. Res. Lett.,* **83,** 765–774.

Goto, H. & Morikawa, H., 2012. Ground motion characteristics during the 2011 off the Pacific coast of Tohoku earthquake, *Soils Found.,* **52,** 769–779.

Haskell, N.A., 1960. Crustal reflection of plane SH waves, *J. geophys. Res.,* **65,** 4147–4151.

Hatayama, K., Kanno, T. & Kudo, K., 2007. Control factors of spatial variation of long-period strong ground motions in the Yufutsu sedimentary basin, Hokkaido, during the Mw 8.0 2003 Tokachi-oki, Japan, earthquake, *Bull. seism. Soc. Am.,* **97,** 1308–1323.

Hauksson, E., Teng, T.L. & Henyey, T.L., 1987. Results from a 1500m deep, three-level downhole seismometer array: site response, low Q values, and fmax, *Bull. seism. Soc. Am.,* **77,** 1883–1904.

Holland, J.H., 1975. *Adaptation in Natural and Artificial Systems: An Introductory Analysis with Applications to Biology, Control, and Artificial Intelligence,* University of Michigan Press, Ann Arbor.

Huang, H.C. & Chiu, H.C., 1996. Estimation of site amplification from Dahan downhole recordings, *Eathq. Eng. Struct. Dyn.,* **25,** 319–332.

Iai, S., Morita, T., Kameoka, T., Matsunaga, Y. & Abiko, K., 1995. Response of a dense sand deposit during 1993 Kushiro-oki earthquake, *Soils Found.,* **35,** 115–131.

Iwaki, A. & Iwata, T., 2010. Simulation of long-period ground motion in the Osaka sedimentary basin: performance estimation and the basin structure effects, *Geophys. J. Int.,* **181,** 1062–1076.

Iwano, S., Fukuda, Y. & Ishiyama, T., 1991. An estimation of fault related structures by means of one-dimensional gravity surveys—case studies at the Katagihara fault and the Fumotomura fault, *J. Geogr.,* **110,** 44–57 (in Japanese with English abstract).

Kagawa, T., Zhao, B., Miyakoshi, K. & Irikura, K., 2004a. Modeling of 3D basin structures for seismic wave simulations based on available information on the target area: case study of the Osaka basin, Japan, *Bull. seism. Soc. Am.,* **94,** 1353–1368.

Kagawa, T., Iemura, H., Irikura, K. & Toki, K., 2004b. Strong ground motion observation by the Commitee of Earthquake Observation and Research in the Kansai Area (CEORKA), *J. Jpn. Assoc. Earthq. Eng.,* **4,** 128–133.

Kansai Geo-informatics Network, 2002., *New Kansai Ground—Kyoto Basin*, Kansai Geo-informatic Network, Osaka (in Japanese).

Kawase, H. & Aki, K., 1989. A study on the response of a soft basin for incident S, P, and Rayleigh waves with special reference to the long duration observed in Mexco city, *Bull. seism. Soc. Am.,* **79,** 1361–1382.

Downloaded from http://gji.oxfordjournals.org/ at Kyoto University Library on July

Kawase, H., 1996. The cause of the damage belt in Kobe: "the basin-edge effect," constructive interference of the direct *S*-wave with the basin-induced diffracted/Rayleigh waves, *Seism. Res. Lett.,* **67,** 25–34.

Kobayashi, K., Amaike, F. & Abe, Y., 1992. Attenuation characteristics of soil deposits and its formulation, in *Proceedings of the International Symposium Effects of Surface Geology on Seismic Motion,* Yokohama, Japan, pp. 269–274.

Kudo, K. & Shima, E., 1970. Attenuation of shear waves in soil, *Bull. Earthq. Res. Inst., Univ. of Tokyo,* **48,** 145–158.

Kurita, T. & Matsui, K., 1997. Sensitivity analysis on measurement noise in the identification of soil properties from vetical array observation data, *Earthquake Engng. Struct. Dyn.,* **26,** 951–965.

Parolai, S., Bindi, D., Ansal, A., Kurtulus, A., Strollo, A. & Zschau, J., 2010. Determination of shallow S-wave attenuation by down-hole waveform deconvolution: a case study in Istanbul (Turkey), *Geophys. J. Int.,* **181,** 1147–1158.

Pozgay, S.H., Wiens, D.A., Conder, J.A., Shiobara, H. & Sugioka, H., 2009. Seismic attenuation tomography of the Mariana subduction system: implications for thermal structure, volatile distribution, and slow spreading dynamics, *Geochem. Geophys. Geosyst.,* **10,** Q04X05.

Satoh, T., Kawase, H. & Sato, T., 1995. Evaluation of local site effects and their removal from borehole records observed in the Sendai region, Japan, *Bull. seism. Soc. Am.,* **85,** 1770–1789.

Sato, H., Kanatani, M. & Ohtori, Y., 2006. Identification of damping factor considering its lower limit by spectral ratio inversion—application to borehole array records at hard rock sites and evaluation of attenuation characteristics, *J. Struct. Constr. Eng. AIJ,* **604,** 55–62 (in Japanese with English abstract).

Seale, S.H. & Archuleta, R.J., 1989. Site amplification and attenuation of strong ground motion, *Bull. seism. Soc. Am.,* **79,** 1673–1696.

Suetomi, I. & Yoshida, N., 1998. Nonlinear behavior of surface deposit during the 1995 Hyogoken-Nambu earthquake, *Soils and Foundations,* **2,** 11–22.

Takemura, M., Ikeura, T., Takahashi, K., Ishida, H. & Ohshima, Y., 1993. Attenuation characteristics of seismic waves in secimentary layers and strong motion estimation, *J. Struct. Constr. Eng. AIJ,* **446,** 1–13 (in Japanese with English summary).

Tsujihara, O. & Sawada, T., 2003. Relation between damping model and accuracy in identification of subsurface ground, *J. Struct. Mech. Earthq. Eng. (I),* **745,** 209–214 (in Japanese with English abstract).

Tsumura, N., Hasegawa, A. & Horiuchi, S., 1996. Simultaneous estimation of attenuation structure, source parameters and site response spectra—application to the northeastern part of Honshu, Japan, *Phys. Earth planet. Inter.,* **93,** 105–121.

Tsumura, N., Matsumoto, S., Horiuchi, S. & Hasegawa, A., 2000. Three-dimensional attenuation structure beneath the northeastern Japan arc estimated from spectra of small earthquakes, *Tectonophysics,* **319,** 241–260.

Uemura, Y., 1990. Tectonic landforms and quanternary tectonics of the western margin of Kyoto basin, southwest Japan, *Ritsumeikan Geogr. Soc.,* **2,** 37–56 (in Japanese).

Wakamatsu, K. & Matsuoka, M., 2006. Development of the 7.5-arc-second engineering geomorphologic classification database and its application to seismic microzoning, *Bull. Earthq. Res. Insts., Univ. Tokyo,* **81,** 317–324.

Wald, D.J. & Allen, T.I., 2007. Topographic slope as a proxy for seismic site conditions and amplification, *Bull. seism. Soc. Am.,* **97,** 1379–1395.

Yamada, K. & Horike, M., 2007. Inference of Q-values below 1 Hz from borehole and surface data in the Osaka basin by three-component waveform fitting, *Bull. seism. Soc. Am.,* **97,** 1267–1278.

Downloaded from http://gji.oxfordjournals.org/ at Kyoto University Library on July 17, 2013